Received 3 December 2021; revised 18 January 2022; accepted 25 January 2022. Date of publication 7 February 2022; date of current version 25 February 2022.

*Digital Object Identifier 10.1109/OJCOMS.2022.3148781*

# Phase Noise Resilient Three-Level Continuous-Phase Modulation for DFT-Spread OFDM

**MARKKU RENFORS [1] (Life Fellow, IEEE), ISMAEL PERUGA NASARRE [1,3], TONI LEVANEN [1,2], KARI PAJUKOSKI [3], AND MIKKO VALKAMA [1] (Fellow, IEEE)**

[1]Department of Electrical Engineering, Tampere University, 33101 Tampere, Finland

[2]Nokia Mobile Networks, 02610 Espoo, Finland

[3]Nokia Bell Labs, 90620 Oulu, Finland

CORRESPONDING AUTHOR: I. P. NASARRE (e-mail: ismael.peruga@tuni.fi)

This work was supported in part by the Academy of Finland under Grant 319994, Grant 338224, and Grant 332361; in part by the Finnish Funding Agency for Innovation under Project ENTRY100GHz; and in part by Nokia Bell Labs.

**ABSTRACT** In this paper, a novel waveform with low peak-to-average power ratio (PAPR) and high robustness against phase noise (PN) is presented. It follows the discrete Fourier transform spread orthogonal frequency division multiplexing (DFT-s-OFDM) signal model. This scheme, called 3MSK, is inspired by continuous-phase frequency shift keying (CPFSK), but it uses three frequencies in the baseband model – specifically, 0 and $\pm f_{\text{symbol}}/4$, where $f_{\text{symbol}}$ is the symbol rate – which effectively constrains the phase transitions between consecutive symbols to 0 and $\pm\pi/2$ rad. Motivated by the phase controlled model of modulation, different degrees of phase continuity can be achieved, allowing to reduce the out-of-band (OOB) emissions of the transmitted signal, while supporting receiver processing with low complexity. Furthermore, the signal characteristics are improved by generating an initial time-domain constant envelope signal at higher than the symbol rate. This helps to reach smooth phase transitions between 3MSK symbols, while the information is encoded in the phase transitions. Also the possibility of using excess bandwidth is investigated by transmitting additional non-zero frequency bins outside the active frequency bins of the basic DFT-s-OFDM model, which provides the capability to greatly reduce the PAPR. The most critical tradeoffs of the oversampled schemes are that improved PAPR is achieved with the cost of somewhat reduced link performance and, in case of excess band, also the spectrum efficiency is reduced. Due to the fact that the information is encoded in the phase transitions, a receiver model that tracks the phase variations without needing reference signals is developed. To this end, it is shown that this new modulation is well-suited for non-coherent receivers, even under strong phase noise (PN) conditions, thus allowing to reduce the overhead of reference signals. Evaluations of this physical-layer modulation and waveform scheme are performed in terms of transmitter metrics such as PAPR, OOB emissions and achievable output power after the power amplifier (PA), using a practical PA model. Finally, coded radio link evaluations are also provided, demonstrating that 3MSK has a similar bit error rate (BER) performance as that of traditional quadrature phase-shift keying (QPSK), but with significantly lower PAPR, higher achievable output power, and the possibility of using non-coherent receivers.

**INDEX TERMS** 5G New Radio evolution, 6G, coverage, DFT-s-OFDM, energy-efficiency, modulation, peak-to-average-power ratio, radio link performance, continuous phase modulation, CPM, constant envelope, spectrum localization.

## I. INTRODUCTION

LOW-POWER wide-area networks (LPWANs) are expected to be one of the fundamental pillars of the upcoming radio technologies [1]–[3], where a high diversity of applications exists, such as smart healthcare, factory automation, smart agriculture, wearable devices or vehicle to vehicle (VTV) communications, to name a few, each with different requirements in terms of latency, reliability and throughput. These discrepancies in requirements call for different types of solutions tailored for each necessity [4]. However, one common requirement from all the types of applications is the need of having low power consumption in the physical (PHY) layer [5], since extended battery lifetime and very wide network coverage are some of the most important parameters for this type of communication.

### A. STATE-OF-THE-ART

The main goals of LPWAN are to offer long range connections with the lowest possible power consumption and cost. To achieve these goals, different approaches can be taken [4] including low peak to average power ratio (PAPR) modulations, resulting in very efficient use of the power amplifier (PA) [6], or narrow-band modulation techniques, which result in low noise power in the receiver, like the approach used in NB-IoT [7]. Other techniques include spread spectrum [8], duty cycling [9] or reducing the control signaling overhead. These techniques have in common the efficient use of the power, and all of them have their drawbacks.

From the previous listed approaches, in this work, a low PAPR modulation is proposed in order to use the PA efficiently and increase the coverage of the network, while not compromising the spectral efficiency.

The presented 3MSK modulation is inspired by the minimum shift keying (MSK) idea, which was developed in [10]. MSK is a continuous phase modulation (CPM), a special form of binary continuous phase frequency shift keying (CPFSK) with a modulation index $h = 1/2$. It also has a linear digital modulation interpretation with a pulse shape of half period of a sinusoid [11]. The term "minimum" in MSK comes from the fact that the two frequencies encoding the data have minimum possible frequency deviation necessary to ensure orthogonality between both binary symbols. The resultant waveform presents a constant envelope. In [12], connections of MSK waveform with quadrature phase-shift keying (QPSK), offset QPSK (OQPSK) and frequency shift keying (FSK) are explained, including the constant envelope properties as well as the error rate performance in relation to binary PSK (BPSK). However, MSK still presents high out-of-band (OOB) emissions, which led to the idea of Gaussian MSK (GMSK) [13] in order to reduce the side-lobes by using a Gaussian low-pass filter prior to the modulation.

Furthermore, the need of having robustness against phase noise (PN) in LPWAN is demonstrated in [14], where a PN compensation method for IoT devices is proposed for the standard for low-rate wireless networks IEEE 802.15.4 [15], where also non-coherent detection to MSK signal is discussed as a way to reduce the power consumption of the receiver.

The most widely studied approach for low-PAPR waveforms is based on the $\pi/2$ phase-rotated BPSK modulation [16], which has well-controlled phase behaviour where the phase rotation between consecutive symbols is $\pm\pi/2$. Due to the benefits of OFDM-based multiple access, $\pi/2$-BPSK is usually considered in the DFT-s-OFDM [17] context, also known as single-carrier frequency-division multiple access (SC-FDMA), which is applied in 4G long-term evolution (LTE), NB-IoT, as well as in 5G New Radio in coverage-limited uplink scenarios. The relationship between CP-OFDM and DFT-s-OFDM lies on the fact that in the DFT-s-OFDM waveform, the QAM symbols to be transmitted within the OFDM-based block undergo a linear DFT precoding operation, which spreads the information in the frequency domain. Following the DFT, the remaining processing blocks of DFT-s-OFDM are the same as those in CP-OFDM. Basically, the concatenated DFT-IFFT operations implement sampling rate conversion (sampling rate increase or interpolation) and bandwidth limitation, along with a frequency shift within the range of IFFT bins. Therefore, the resulting transmit signal is a single-carrier signal with relatively low PAPR. In basic form, the DFT-s-OFDM signal is transmitted in the minimum number of frequency bins (or resource elements (REs) in 3GPP terminology), which is equal to the number of single-carrier (usually QAM) symbols allocated to a DFT-s-OFDM block. This corresponds to zero roll-off in traditional single-carrier transmission schemes. However, both in traditional single carrier and DFT-s-OFDM cases, the signal characteristics, primarily PAPR and OOB emissions, can be greatly improved by using excess bands. Then the number of active frequency bins is higher in the DFT-s-OFDM model. In this context, frequency-domain spectrum shaping (FDSS) [6] is commonly applied, corresponding to Nyquist pulse shaping. This means that the frequency bins generated by DFT are copied symmetrically over the excess bands on both sides (corresponding to up-sampling in time-domain multi-rate signal processing), and then the used DFT bins are weighted, e.g., by a raised cosine (RC) type function. Various schemes for optimizing the FDSS weights have been presented in the literature, see [18] and references therein. These papers indicate clearly that the RC-type filters are not necessarily optimal for FDSS-based low-PAPR schemes.

The block structure of OFDM based waveforms introduces abrupt transitions between OFDM blocks and also between the main OFDM block and its cyclic prefix (CP). This is particularly an issue in DFT-s-OFDM signals with well-controlled amplitude and phase behavior, such as $\pi/2$-BPSK, CPSK [19], and 3MSK, which can be considered as nearly constant-envelope (CE) waveforms. Therefore, methods to guarantee smooth/continuous phase behavior between (i) CP-OFDM blocks and (ii) between main OFDM block and its CP have been considered in the literature

for CPM-based DFT-s-OFDM and $\pi/2$-BPSK in particular, see [20] and references therein.

The idea of constraining the phase transitions between consecutive PSK symbols with the goal of reduced PAPR was studied in [19], where a constrained PSK (CPSK) modulation was presented for DFT-s-OFDM. For CPSK, an underlying PSK constellation is defined, and for every transmitted symbol, only a smaller set of the constellation symbols are available for transmission. In non-oversampled cases, 3MSK can also be seen as a special case of constrained PSK with an underlying constellation of QPSK and three alternatives for each transmitted symbol. However, in this paper we present various additional features, including oversampled signal generation, excess band utilization, as well as application and analysis of different signal phase continuity aspects.

### B. CONTRIBUTIONS AND ORGANIZATION

DFT-s-OFDM based low-PAPR schemes have focused on binary modulation because it is difficult/impossible to reach the targeted PAPR and OOB characteristics with low/modest complexity with four or more modulation levels. Using 3-level modulation is unconventional, but it can offer good tradeoffs for the signal characteristics while supporting 50% higher spectrum efficiency than binary schemes. Maximizing the bit-rate with 3-level modulation becomes complicated in terms of bit-to-symbol mapping, but transmitting 3 bits in 2 symbols is straightforward and fairly close to the maximum rate, so it is followed also in this paper. It brings some redundancy in bit mapping which can be used to enhance link performance, basically through high-rate trellis coding and relatively simple sequence detection on the receiver side.

In this paper, we propose a novel modulation scheme for DFT-s-OFDM transmission, named as 3MSK, which allows to control the PAPR and OOB emissions by means of different parameterization alternatives concerning oversampled signal generation, imposed phase continuity, as well as the possibility of transmissions using excess bandwidth (EBW). Furthermore, thanks to the phase transition model of 3MSK, we present a receiver model capable of tracking and compensating PN effects without the need of extra reference signals, thus reducing the reference signal overhead. Finally, we also demonstrate that the proposed modulation can be detected with a non-coherent receiver.

The novel contributions of this paper include:

- A DFT-s-OFDM based 3-level continuous phase modulation scheme with nearly constant envelope is proposed.
- Analysis of trellis-based bit-to-symbol mapping alternatives.
- Schemes for phase continuity (i) between main OFDM block and its CP and (ii) between OFDM blocks are developed and shown to provide significant reduction in OOB emissions. For (i) we adapt the model used earlier for $\pi/2$-BPSK to 3MSK. For (ii) a novel scheme based on multiples of $\pi/2$ phase rotations of CP-OFDM blocks is proposed, considering also the required receiver processing. The benefits of both elements are evaluated, leading to clear recommendations of their use.
- Oversampled initial 3MSK signal generation based on phase interpolation is proposed and its capability of significant PAPR reduction is demonstrated, considering also its effects on OOB emissions and link performance.
- The use of excess band together with the oversampled model is proposed and demonstrated to provide significant further reduction of PAPR. In this paper, we consider also a scheme where the excess band is applied only on the transmitter side and the receiver does not make use of it. This makes it possible for adjacent users to have fully or partly overlapping excess bands. This reduces the related spectrum overhead up to 50% when adjacent users' excess bands are fully overlapping.
- Tracking of the phase error due to large PN effects without explicitly using reference signals is developed and demonstrated. This reduces the signaling overhead for obtaining good PN compensation.

Naturally, these benefits come with certain tradeoffs concerning different performance metrics and signal processing complexity, which are summarized in the Conclusions section.

It should be mentioned that in this paper the DFT-s-OFDM is considered only as a central element of the modulation scheme, while the focus is on low-power user devices. The FDMA aspect becomes relevant in scenarios where a base-station is simultaneously receiving signals from multiple devices. The use of DFT-s-OFDM approach leads to highly flexible uplink multiple access which can be configured to reach compatibility with widely-deployed OFDM or DFT-s-OFDM systems.

The rest of the paper is organized as follows: In Section II, the 3MSK signal model and transmitter architecture are introduced, including the trellis-based bit-to-symbol mapping, phase continuity model, as well as oversampled signal and excess band generation. Section III focuses on the effects and usage of excess band and Section IV explains the receiver signal processing architecture, with focus on 3MSK signal detection. Section V introduces the performance metrics used for evaluation, and the numerical results and comparisons are included in Section VI. Finally, the concluding remarks can be found in Section VII.

## II. TRANSMITTER PROCESSING

3MSK is a modulation tailored for single carrier waveform that allows for lower PAPR, low OOB emissions, robustness against the effects of PN and can be utilized with non-coherent detection.

Traditional MSK [12] is a binary modulation scheme using two frequencies $+f_{\text{symbol}}/4$ and $-f_{\text{symbol}}/4$, where $f_{\text{symbol}}$ is the symbol rate. Phase continuity is enforced between consecutive symbols. During each symbol interval

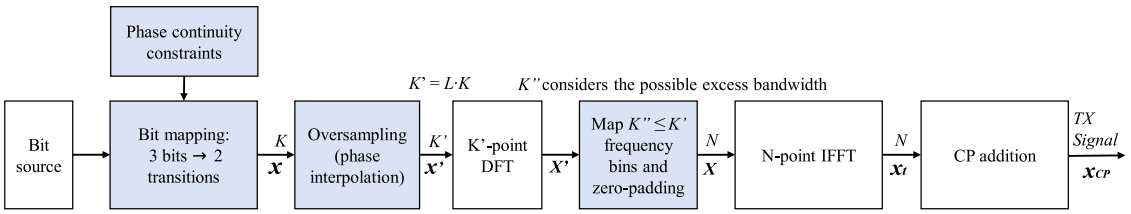


**FIGURE 1.** Block diagram of the generic 3MSK transmitter for DFT-s-OFDM.

of length $T_{\text{symbol}} = 1/f_{\text{symbol}}$, a phase rotation of $\pm T_{\text{symbol}} \cdot 2\pi f_{\text{symbol}}/4 = \pm\pi/2$ rad takes place in the baseband model. In the DFT-s-OFDM context, $f_{\text{symbol}}$ depends on the allocation bandwidth as discussed below.

3MSK can be considered as an extension of MSK modulation with additional zero-frequency as the third symbol in the baseband FSK model. The three frequencies allowed to be transmitted per symbol interval effectively constrain the phase transitions between consecutive symbols to $0, +\pi/2$ and $-\pi/2$ rad. At symbol rate, this can be seen as QPSK modulation excluding 180 degree phase rotation between consecutive symbols. While MSK has also an interpretation as linear digital modulation (OQPSK with specific pulse shape [12]), 3MSK doesn't have simple linear digital modulation interpretation in oversampled discrete-time or continuous-time domains.

In the basic DFT-s-OFDM case without oversampling, the constrained QPSK interpretation is valid, and the scheme follows the orthogonal DFT-s-OFDM principle and provides intersymbol interference (ISI) -free transmission in the absence of dispersive channel. In the oversampled case of this paper, the core idea is to interpolate the phase between symbol instants, while the amplitude remains exactly constant at the DFT input. A straightforward approach is to use linear interpolation of phase, which corresponds to the use of the mentioned three FSK frequencies, but we consider also using a low-order interpolation filter providing smoothed phase transitions. Naturally, the DFT-s-OFDM transmitter processing limits the signal bandwidth, degrading the constant envelope property, but in the oversampled case we can expect less degradation than in the non-oversampled model. Furthermore, the use of excess band can be expected to further reduce the degradation.

Fig. 1 shows the block diagram of the transmitter, highlighting in blue the main processing blocks for 3MSK. Fig. 2 shows the in-phase/quadrature (IQ) scatterplots of the 3MSK signal compared to QPSK. It can be seen that by restraining the phase transitions between consecutive symbols to $\pm\pi/2$ or 0 rad in the 3MSK modulation, the zero-crossings in the scatter-plot can be avoided, and therefore the signal does not present samples with very low power, in contrast to QPSK, where samples with low power appear in the zero-crossings, and samples with larger power than in the 3MSK are also present, increasing the PAPR of the signal.

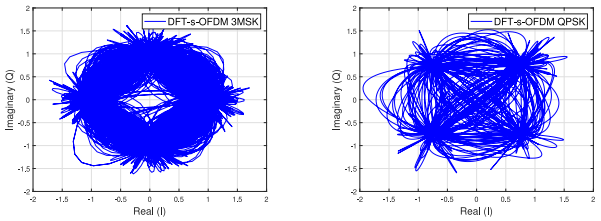


**FIGURE 2.** IQ scatterplot of (a) the 3MSK signal without oversampling and phase continuity options, and (b) DFT-s-OFDM based QPSK signal.

### A. SYSTEM MODEL

Let us first define the basic quantities for presentation clarity. The mapping of bits to 3MSK symbols can be done by means of the so-called 3MSK block. A 3MSK block is a block of 3MSK symbols that follow the constraint of phase difference between consecutive symbols and encode the information in their phase transitions. $B$ bits are mapped to $K$ 3MSK symbols to form a 3MSK block.

In traditional DFT-s-OFDM processing, the number of symbols carried by a DFT-s-OFDM block is the same as the DFT size in the modulator, and therefore corresponds to the size of the in-band, or active frequency bins. With this parameterization, $K$ 3MSK symbols are generated for each OFDM block, and the effective 3MSK symbol rate is $f_{\text{symbol}} = K/(N + N_{\text{CP}}) \cdot f_{\text{S}}$, where $N_{\text{CP}}$ is the CP length and $f_{\text{S}}$ is the sampling rate after the IFFT and CP insertion.

The number of bits $B$ of a 3MSK block can be up to $3K/2$ if no other constraints than the phase difference between symbols are applied. However, as will be seen in the following sub-sections, if phase continuity between cyclic prefix (CP) and main block should be achieved, 2 bits less are mapped. After obtaining the $K$ 3MSK symbols, interpolation (sampling rate increase) by a factor of $L \geq 1$ (typically $L = 2$) may be performed, giving $K' = L \cdot K \geq K$ samples to be used as input to the DFT of size $K'$. Finally, $K''$ DFT bins are mapped to the IFFT input. In oversampled cases, i.e., with $L > 1$, an excess band of $E \in [0, N - K']$ frequency bins may be included in the mapping, such that

$$K'' = K + E. \tag{1}$$

The excess bandwidth (EBW) can also be denoted as EBW $= 100 \cdot E/K$ %.

These processing steps can be interpreted as FDSS, possibly with excess band, using rectangular window for weights.

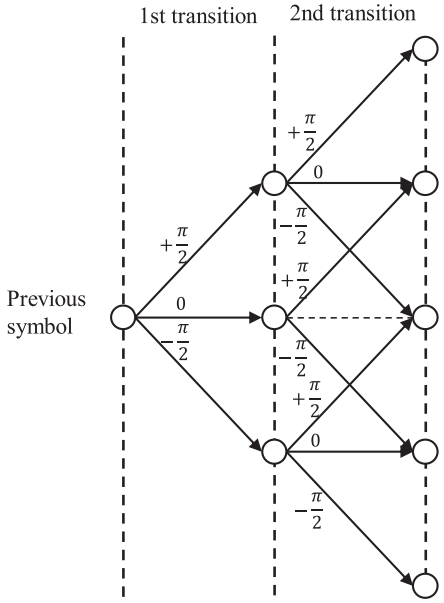


**FIGURE 3.** Example of a symmetric structure of bit-to-transition mapping. 3 bits are mapped to 8 different transitions (2 consecutive 0 rad transitions is avoided).

While this is straightforward from the implementation point of view, we have not been able to obtain significant improvement in signal characteristics or link performance using other window shapes.

In the bit mapping, 3 bits are mapped into 2 consecutive transitions. This means that each 3MSK symbol carries 1.5 bits. Since 2 consecutive transitions carry the 3 information bits, and the transitions can be either $0, +\pi/2, -\pi/2$, there would be 9 different transition combinations. Because 3 bits encode 8 different values, one transition combination needs to be avoided. This is illustrated in Fig. 3 showing possible transition pairs, avoiding the two consecutive 0 rad transitions. Within this paper, this type of mapping is referred to as symmetric mapping (SM). It has to be noted that any of the possible transitions in the second rotation can be discarded, possibly generating a non-symmetric mapping (NSM). We have observed that non-symmetric mappings may provide slightly lower PAPR and OOB emissions than the symmetric mapping. However, in the continuation, we mainly consider symmetric mapping due to its simplicity.

Table 1 shows an example of a bit-to-transition mapping table that was found after an exhaustive search over all valid symbol sequences of 4 symbols (6 bits), based on Hamming distance and Euclidean metric for the symmetric mapping. The idea is to minimize the bit error probability by minimizing the Hamming distance (number of different bits) of sequences having small Euclidean distance. It needs to be noted that there are multiple optimum mappings that provide the same metric as the mapping of the example. Furthermore, it is clear from the nature of the mapping (bit-to-transition) that it is in fact a differential mapping, where the information is carried in the phase transitions, hence allowing for non-coherent detection.

**TABLE 1.** Example of bit-to-transition mapping after exhaustive search over all valid sequences of 4 symbols.

| b2 | b1 | b0 | First transition [rad] | Second transition [rad] |
|---|---|---|---|---|
| 0 | 0 | 0 | $-\frac{\pi}{2}$ | $+\frac{\pi}{2}$ |
| 0 | 0 | 1 | $+\frac{\pi}{2}$ | $-\frac{\pi}{2}$ |
| 0 | 1 | 0 | $-\frac{\pi}{2}$ | 0 |
| 0 | 1 | 1 | 0 | $-\frac{\pi}{2}$ |
| 1 | 0 | 0 | 0 | $+\frac{\pi}{2}$ |
| 1 | 0 | 1 | $+\frac{\pi}{2}$ | 0 |
| 1 | 1 | 0 | $-\frac{\pi}{2}$ | $-\frac{\pi}{2}$ |
| 1 | 1 | 1 | $+\frac{\pi}{2}$ | $+\frac{\pi}{2}$ |

After summarizing the basic characteristics of the 3MSK, let us further explain the additional properties that this modulation can support in order to reduce PAPR and OOB emissions: (i) enhanced phase continuity and (ii) oversampled transmission, with the possibility of employing excess bandwidth.

### *B. PHASE CONTINUITY*

The controlled phase transition model of the 3MSK allows us to have phase continuity between the CP and the main block (i.e., within a DFT-s-OFDM block) as well as between consecutive CP-OFDM blocks. It is possible to use either of the two elements of phase continuity, but combining the two (called full phase continuity) gives the maximum reduction of the OOB emissions, as will be seen in Section VI.

#### 1) PHASE CONTINUITY BETWEEN CP AND MAIN BLOCK

In the context of phase continuity, we should consider the cyclic nature of the high-rate DFT-s-OFDM signal, noting that the DFT-IFFT process interpolates $N/K - 1$ samples between the 3MSK symbol instants. We adopt the model that the first sample of the DFT-s-OFDM block is the first transmitted 3MSK symbol. Then the last transition ends at the first sample of the block, i.e., the first 3MSK symbol, which is not included in the block. The final state of the last transition is referred to as the end-phase of the 3MSK block, and it is equal to the initial phase, but it is not transmitted in the block. We can see that some degree of phase continuity between CP and the main DFT-s-OFDM symbol is achieved automatically, i.e., the end-phase of CP is equal to the initial phase of the main block. However, without additional constraints, the phase of the last 3MSK symbol of the block could be any multiple of $\pi/2$, and the final phase transition could be $\pi$ rad.

The phase continuity between CP and the main block can be enhanced by forcing the end-phase of the 3MSK block to be equal to the initial phase, in which case the last transition follows the 3MSK rule. This is obtained, for example, by generating $K + 1$ 3MSK symbols, forcing the first and last symbols of the block to be the same, and just transmitting $K$ first symbols. This model is referred to as CP phase continuity in the following discussions.

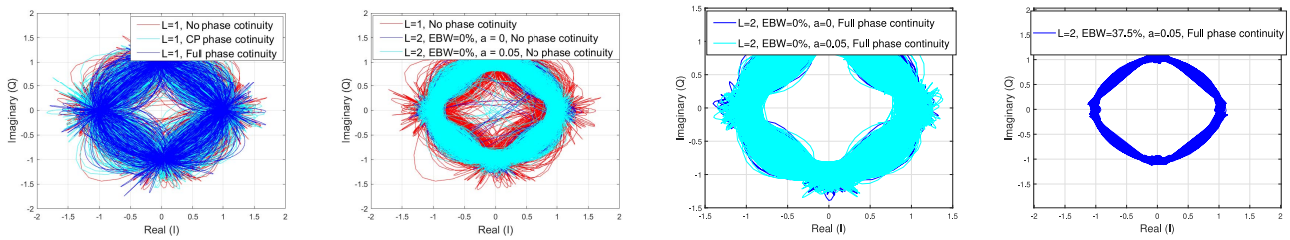


**FIGURE 4.** Effects of oversampling factor ($L$), excess band, and phase continuity options on the scatter plot of 3MSK. (a) $L = 1$ and different phase continuities, (b) $L = 1$ and $L = 2$ comparison without phase continuity, (c) $L = 2$ with $a = 0$ and $a = 0.05$ comparison with full phase continuity, and (d) $L = 2$ with 37.5% EBW.

Fig. 4(a) shows the scatterplot of the signal when phase continuity between CP and main block is used, compared to the case without forcing phase continuity and the full phase continuity case, that will be explained in the following section. It can be seen that when CP phase continuity is added, the number of zero crossings caused by phase variations of $\pi$ rad is reduced. However, there are still some phase transitions larger than $\pi/2$ rad that are caused by the phase discontinuity between CP-OFDM blocks.

Assuming that the 3MSK block size is the same as the number of symbols in a DFT-s-OFDM block, $K$, 2 bits of data per 3MSK block are lost. This is because to start and end in the same phase, only 1 bit, instead of 3, can be mapped to the last 2 transitions. The bit-to-transition mapping of the last symbol of a 3MSK block depends on the phase state before the last pair of transitions, and there are 4 possible phases that could have been transmitted in the symbol before the last two transitions. These phases are $0, \pi/2, \pi$ and $-\pi/2$ rad. The last bit can be either 0 or 1. This leaves us with 8 possible transitions to which the last bit can be mapped, which allows us to use a similar bit-to-transition mapping table as Table 1. This is a useful property of using the symmetric bit-to-transmission mapping, because if a non-symmetric mapping were to be used, it would not be possible to use the same table to obtain CP phase continuity.

By including the phase continuity constraint between CP and main block, the 3MSK block maps $3K/2 - 2$ bits to $K$ 3MSK symbols. Assuming that the initial and end phase states are the zero phase (0 rad), the bit-to-transition mapping table of the last bit to provide phase continuity between CP and main block is shown in Table 2.

This type of phase continuity helps in the receiver processing, since it can be assumed that the first and last state of the receiver trellis are the same, thus the selection of the maximum likelihood (ML) or maximum a posteriori (MAP) sequence by the detector is determined by the path that has the lowest metric with the same initial and end state.

**TABLE 2.** Example of last bit-to-transition mapping to obtain phase continuity between CP and main block.

| Bit | Phase transmitted before last symbol [rad] | First transition [rad] | Second transition [rad] |
|---|---|---|---|
| 0 | 0 | $-\frac{\pi}{2}$ | $+\frac{\pi}{2}$ |
| 1 | 0 | $+\frac{\pi}{2}$ | $-\frac{\pi}{2}$ |
| 0 | $+\frac{\pi}{2}$ | $-\frac{\pi}{2}$ | 0 |
| 1 | $+\frac{\pi}{2}$ | 0 | $-\frac{\pi}{2}$ |
| 0 | $-\frac{\pi}{2}$ | 0 | $+\frac{\pi}{2}$ |
| 1 | $-\frac{\pi}{2}$ | $+\frac{\pi}{2}$ | 0 |
| 0 | $\pi$ | $-\frac{\pi}{2}$ | $-\frac{\pi}{2}$ |
| 1 | $\pi$ | $+\frac{\pi}{2}$ | $+\frac{\pi}{2}$ |

### 2) PHASE CONTINUITY BETWEEN CONSECUTIVE DFT-S-OFDM BLOCKS

Fig. 4(a) shows the IQ scatterplot of the signal also when both phase continuity between consecutive DFT-s-OFDM blocks and between the CP and the main block are used (denoted as full phase continuity). It can be seen that in this case there are no abrupt phase transitions, while in the other two cases, phase transitions larger than $\pi/2$ between consecutive samples exist.

Phase continuity between consecutive DFT-s-OFDM blocks can be achievable in two different ways. One alternative is to force the state sequence of the first sample of the CP to to match the end state of the previous 3MSK block. This approach is equivalent to the one used to generate phase continuity between CP and main block, and has the drawback that another 2 bits per DFT-s-OFDM block are lost.[1]

Alternatively, it is also possible to compensate the phase rotations during each underlaying CP-OFDM block in such a way that the phase continuity is achieved between the first sample of the CP and the end-phase of the previous DFT-s-OFDM block, as illustrated in Fig. 5. In this approach, the loss of two additional bits is avoided. Given that $\phi_{t-1}^{\text{last}}$ is the end-phase of block $t-1$, and the phase of the first sample of the CP of the current block ($t$) is $\phi_t^{\text{first}}$, the phase difference is

$$\phi_t^{\text{diff}} = \phi_{t-1}^{\text{last}} - \phi_t^{\text{first}}. \tag{2}$$

1. Similar approach has been used earlier with $\pi/2$ BPSK for both types of phase continuity [20].

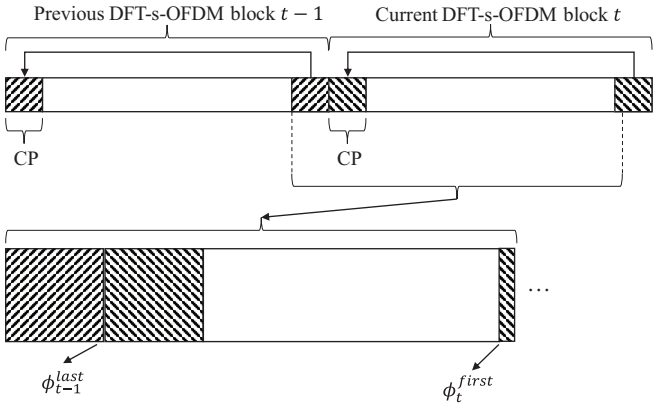


**FIGURE 5.** Phase continuity between consecutive DFT-s-OFDM blocks.

Then the block $t$ is rotated by $u\frac{\pi}{2}$ rad, where $u$ is the integer that satisfies

$$\min_u \left| u\frac{\pi}{2} - \phi_t^{\text{diff}} \right|. \tag{3}$$

It is important to notice that applying CP phase continuity enhances the block phase continuity characteristic by forcing the last transition of the block to follow the 3MSK rule, as discussed above.

It has to be noted that depending on the numerology used, when the CP-length is formed by an integer number of 3MSK symbols, the phase difference $\phi_t^{\text{diff}}$ will already be an integer multiple of $\pi/2$ rad. In the other cases when the CP-length is not formed by an integer number of 3MSK symbols, the phase continuity between DFT-s-OFDM blocks is not exact. It can be noted that the same constraints on numerology for exact phase continuity apply also for the controlled state sequence based method mentioned above. Simulations of Section VI confirm that exact block phase continuity has clear benefit over approximate phase continuity, and that CP length being exact multiple of the 3MSK symbol duration is sufficient, even if the DFT-s-OFDM main block duration is not a multiple of the IFFT output sampling interval.

The phase continuity between DFT-s-OFDM blocks allows to reduce the OOB emissions, and the combination with CP-main block phase continuity brings the largest OOB emission reduction.

### C. OVERSAMPLED 3MSK SIGNAL AND EXCESS BAND GENERATION

The 3MSK signal can be generated at higher than symbol rate, which allows for reduction of the PAPR. In this paper, we focus on the oversampling factor of $L = 2$. The effects of the oversampling can be seen in Fig. 4, where Fig. 4(a) shows the non oversampled version and Fig. 4(b), Fig. 4(c), and 4(d) show the scatterplots of oversampled signals. It can be seen that in the oversampled cases, the signal stays closer to the unit circle, meaning that the power variations are smaller in comparison to the non oversampled case.

Generally, oversampling a signal by $L$ is a sampling rate conversion (interpolation) process where the sample rate is first increased by adding $L-1$ zeros after each incoming sample and filtering the resulting signal by a linear digital finite impulse response (FIR) filter. Here we apply interpolation to the phase sequence of the 3MSK block. In Section VI it will be shown that phase interpolation gives clearly better PAPR and OOB emission characteristics than interpolation of the complex 3MSK symbol sequence, at least when low-order interpolation filters are considered. Phase interpolation maintains the perfectly constant envelope characteristic of the initial 3MSK block.

It is important to apply the phase interpolation to the unwrapped phase sequence, in which case the differences between consecutive phase values represent the intended phase transitions.

We focus on the case with $L = 2$ and consider 7-tap linear-phase (symmetric) FIR filters satisfying two natural constraints: (i) input samples are not affected, (ii) a constant input sequence results in a constant interpolated output sequence. Constraint (i) is satisfied only by a Nyquist-type filters with zero-valued odd taps, except for the one-valued center tap. Then constraint (ii) is satisfied only by impulse responses of the form

$$\mathbf{h} = [-a, 0, 0.5 + a, 1, 0.5 + a, 0, -a]^{\text{T}} \tag{4}$$

with single adjustable parameter, $a$, which affects the smoothness of the interpolated phase function.

With $a = 0$, this corresponds to 3-tap linear interpolation of phase between two consecutive 3MSK symbols.

Values of $a > 0$ provide smoothed phase transitions with some benefits in terms of bit error rate (BER) performance, PAPR, and OOB emissions, as will be seen in Section VI. The process is explained in more details in Section II-D.

Fig. 4(b) shows the difference in the scatterplot for the signal without oversampling and the oversampled signal with different values of the parameter $a$ without imposing any phase continuity, and Fig. 4(c) shows the scatterplots of oversampled signal with different values of $a$ and full phase continuity. The value of $a = 0.5$ is found to be close to optimal for all considered metrics and it is used in later results, along with $a = 0$. It can be seen that the effects of different $a$ values in the scatterplot are rather limited, and therefore we cannot expect great benefits in terms of PAPR.

As will be seen in Section VI, generating the 3MSK symbols at a higher rate helps decreasing the PAPR of the signal and affects the OOB emissions. After the oversampling and interpolation, the length of the 3MSK block is now $L \cdot K$ and a $L \cdot K$-size DFT is then performed before the frequency bin mapping.

Fig. 6 shows the impulse response of DFT-s-OFDM (from the DFT input to the receiver's IDFT output) when 2-times oversampling is used with EBW=0%. It can be seen that at the original symbol-time instants (red samples), the transmission is inter-symbol interference (ISI) free since none of the symbols except the current one have impact, while the inclusion of the interpolated samples (blue samples) generate ISI, with the value of their impact decreasing at both

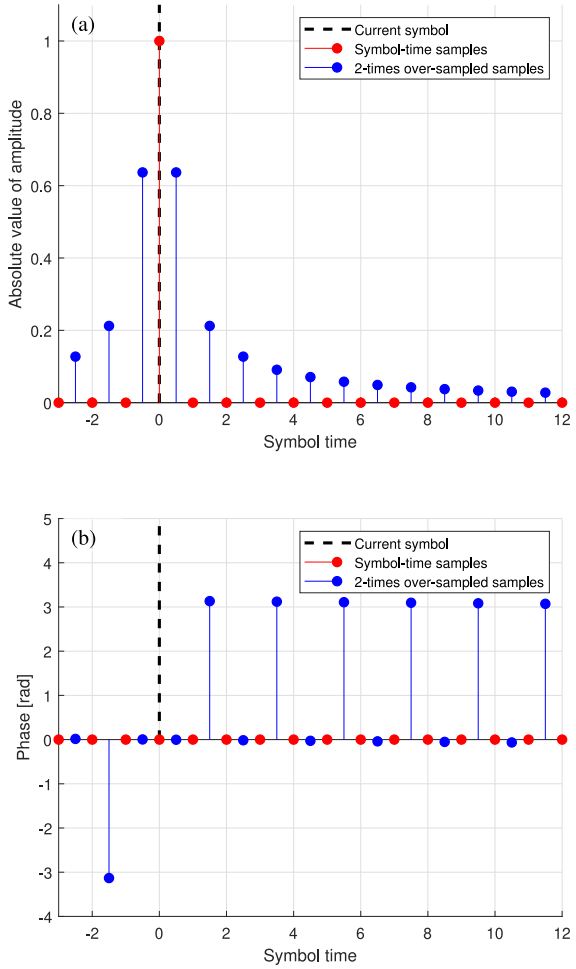


**FIGURE 6.** Illustration of the effects of 2-times oversampling on the impulse response of DFT-s-OFDM for (a) the amplitude response and (b) phase response.

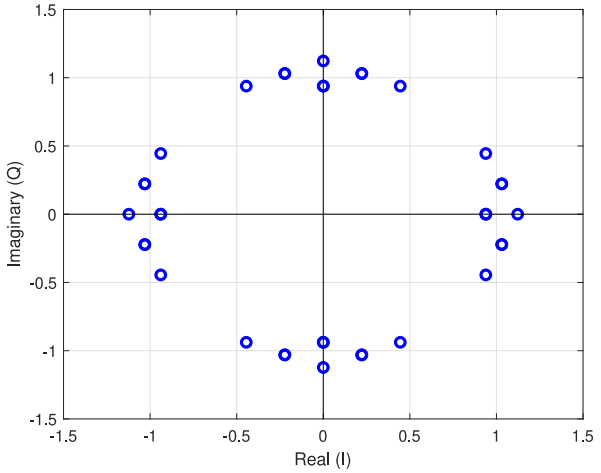


**FIGURE 7.** 3MSK symbol constellation using 3-tap ISI model with 2x oversampled transmitter without excess band and $a = 0$.

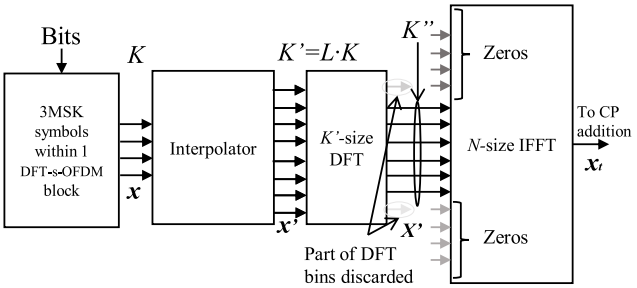


**FIGURE 8.** Diagram example of oversampled transmission with excess band. EBW is tuned by setting some of the DFT bins at the edges to zero.

sides of the current symbol. The inclusion of these blue samples helps to lower the PAPR, but deteriorates the receiver performance due to the added ISI.

The impulse response samples at $-1$ and $+1$ introduce quite significant ISI on the 3MSK symbols. Since this appears in combination with the phase interpolation, this interference is strongly correlated with the symbols. Therefore, analytical study of these effects is fairly complicated and remains as an important topic for future studies, and we include here only numerical evaluation of these effects. Fig. 7 shows the signal values at symbol times after phase interpolation by the basic linear interpolator ($a = 0$) and the DFT-s-OFDM process with a non-oversampled receiver in the absence of the other ISI taps and the noise and channel effects. We can see that the ISI due to taps $\pm 1$ affects mostly the symbol phases, which helps to maintain nearly constant envelope. Assuming unit magnitude after phase interpolation and ignoring the effect of the other ISI taps, the mean value of an observed symbol is found to be 2.02 times the corresponding transmitted symbol. The mean-squared error (MSE) of the ISI-affected symbol constellation is found to be 0.286, and the additional MSE due to the other taps of the impulse response is found to be 0.189. Then the total MSE due to ISI is 0.475. With the assumption that the ISI is Gaussian distributed, the corresponding SNR loss at 3 dB SNR level would be about 1.15 dB. It should be noted that the ISI distribution is far from Gaussian, especially the part that is due to the two strongest ISI taps. Anyway, the numerical results of Section VI follow surprisingly well this model as the corresponding SNR loss is found to be 0.93 dB.

Due to the fact that a larger DFT size is used, more than $K$ frequency bins (also referred as subcarriers) can be used for the transmission. This allows us to use excess band, where at least a portion of the frequency bins apart from the in-band $K$ frequency bins can be allocated in the transmission, while the rest of the frequency bins remain empty. Fig. 8 shows an example of how the frequency bins are obtained and allocated for different excess band configurations. Fig. 4(d) shows the effects of using 37.5% of excess bandwidth (EBW) in the IQ scatterplot of the signal (the percentage of EBW is computed as the number of extra active frequency bins with respect to the in-band frequency bins, as in (1)). It can be seen that by using EBW, the signal envelope is even more confined compared to the case where no EBW is used, lowering the PAPR.

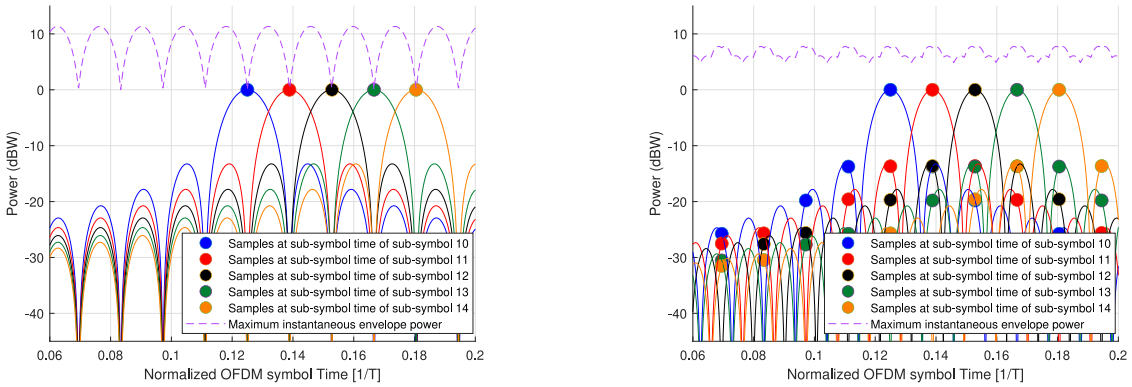


**FIGURE 9.** Dirichlet pulses for symbols number 10 to 14 within a DFT-s-OFDM block with $N = 1024$ for (a) DFT-s-OFDM without excess bandwidth, $K = K'' = 72$, (b) DFT-s-OFDM with excess bandwidth, $K = 72$, $K'' = 96$.

### D. SUMMARY OF TRANSMITTER PROCESSING

The transmitter processing can be summarized with some more details as follows:

1) Bit-to-symbol mapping is implemented according to Table 1, using Table 2 for the last 3MSK symbol of the block in case of CP phase continuity, resulting in $K$-element phase sequence vector $\boldsymbol{\phi}$ with elements $\phi_k$, $k = 0, \ldots, K-1$.
2) In case of oversampling, phase interpolation by the factor $L = 2$ is carried out. Assuming that the impulse response $\mathbf{h}$ of (4) is used, the phase sequence needs to be cyclically extended by one sample in the beginning and end. (In case 3-tap linear interpolation, this is not needed.) The resulting phase vector is unwrapped such that the phase differences between consecutive samples represent the intended phase transitions. Sampling rate is increased by the factor of two by adding zeros between the existing samples. Finally, the extended phase vector is convolved with $\mathbf{h}$ and the result is shortened to length $K' = 2K$ vector $\boldsymbol{\phi'}$ by removing 4 elements from both sides. In case of no oversampling $\boldsymbol{\phi'} = \boldsymbol{\phi}$.
3) Creating complex 3MSK block $\mathbf{x}'$ consisting of elements $x'_k = \exp(j\phi'_k)$, for $k = 0, \ldots, K'-1$.
4) Taking $K'$-point DFT: $\mathbf{X}' = \mathrm{DFT}(\mathbf{x}')$.
5) Mapping $K'' \leq K'$ DFT bins from $\mathbf{X}'$ to the IFFT input vector $\mathbf{X}$ with elements

$$X_l = \begin{cases} X'_l & \text{for } l = 0, \ldots, K''/2-1 \\ 0 & \text{for } l = K''/2, \ldots, N-K''/2-1 \\ X'_{l-N+K'} & \text{for } l = N-K''/2, \ldots, N-1. \end{cases} \quad (5)$$

   This generates DC-centered signal for carrier modulation in later stages of the transmitter. In case of frequency-multiplexing of different user signals, the mapping of DFT bins can be adjusted for another set of IFFT bins.
6) Taking $N$-point IFFT: $\mathbf{x}_t = \mathrm{IFFT}(\mathbf{X})$.
7) Inserting CP to generate a CP-OFDM block $\mathbf{x}_{\mathrm{CP}}$ of $N + N_{\mathrm{CP}}$ samples.
8) In case of block phase continuity: Rotate the generated CP-OFDM block according to Eq. (3) to obtain the baseband signal to be transmitted: $\mathbf{x}_{\mathrm{TX}} = \exp(ju\frac{\pi}{2}) \cdot \mathbf{x}_{\mathrm{CP}}$. Here $u$ depends on the end phase of the previous CP-OFDM block and the initial phase of current CP-OFDM block. For first CP-OFDM block of a transmission frame, $u = 0$. In case of no block phase continuity, $\mathbf{x}_{\mathrm{TX}} = \mathbf{x}_{\mathrm{CP}}$.

## III. USAGE AND EFFECTS OF EXCESS BAND

For DFT-s-OFDM, the effective pulse shape is a Dirichlet function. Following a similar approach as in [6], the DFT-s-OFDM block after the DFT, frequency bin allocation and IFFT (before the CP addition and potential phase rotation to obtain phase continuity) can be expressed as

$$x(n) = \frac{1}{\sqrt{K}} \sum_{k=0}^{K-1} x'_k \underbrace{\frac{1}{\sqrt{N}} \sum_{l \in \mathcal{K}} e^{j\frac{2\pi l}{N}\left(n-\frac{kN}{K}\right)}}_{g\left(n-\frac{kN}{K}\right)}, \quad (6)$$

for $n \in \{0, 1, \ldots, N-1\}$ where $\mathcal{K}$ is the set of frequency bins allocated at the input of the IFFT, of cardinality $K''$, $x'_k$ is the $k$th 3MSK symbol of the $K$-symbol block. The pulses follow the expression

$$g(v) = \frac{1}{\sqrt{N}} e^{-j\frac{\pi v}{N}} \frac{\sin\left(\frac{\pi K v}{N}\right)}{\sin\left(\frac{\pi v}{N}\right)}. \quad (7)$$

It is clear form (6) that the symbols $x'_k$ modulate time-shifted copies of $g(v)$, and the resultant time-domain waveform is the addition of all these modulated pulses.

To exemplify the effects of the excess bandwidth, we can take a look at Fig. 9, where for simplicity only 5 pulses are shown. Fig. 9(a) shows the effective pulses of DFT-s-OFDM when no excess bandwidth is used (72 symbols are sent in 72 frequency bins), and Fig. 9(b) shows the same case

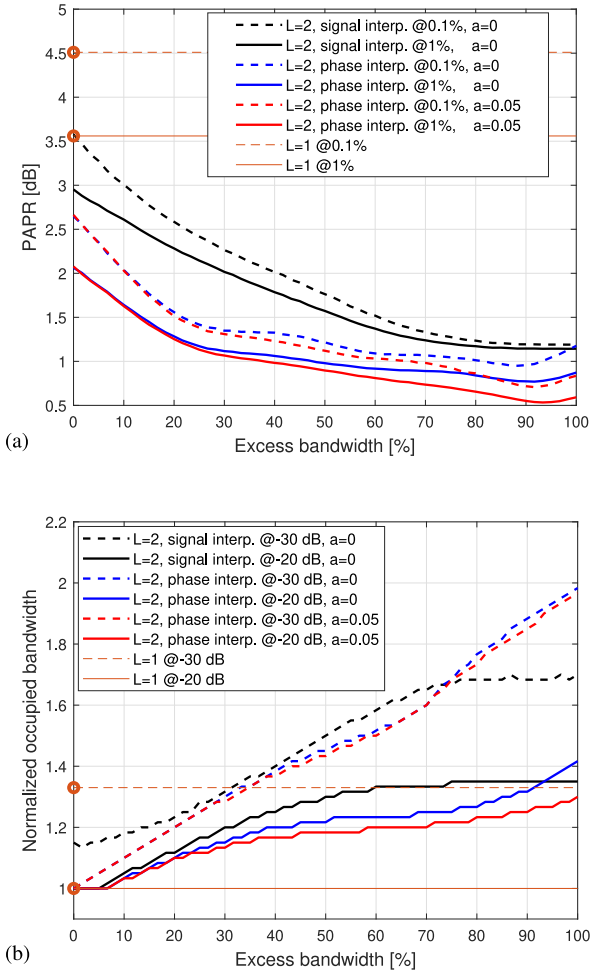


**FIGURE 10.** Illustration of the effects of 2-times oversampling on (a) PAPR vs. EBW and (b) occupied bandwidth vs. EBW.

when excess bandwidth is used (72 symbols are carried in 96 frequency bins). The spectral efficiency in the second case is reduced. It can be seen in the figures that the shape of the pulses is different, while the distance between them remains the same since the same amount of information is sent. The purple line on top of the pulses corresponds to the maximum achievable instantaneous power, which is the case when the pulses are added up coherently, producing peaks. It is clear from the figures that the maximum peaks are larger in the case without excess bandwidth, and therefore, the PAPR would be higher. Having larger bandwidth, the sidelobes of the pulses affect less to the neighboring pulses.

Next we evaluate the effect of excess bandwidth on PAPR and occupied bandwidth with $N = 1024$ and $K = 120$, full phase continuity, and $a = \{0, 0.05\}$.The occupied bandwidth is defined as the bandwidth containing 99% or 99.9% of the total transmission power for $-20$ dB or $-30$ dB OOB emission levels, respectively. It is then normalized to the nominal bandwidth of the signal (i.e., $K \cdot SCS$, where $SCS$ is the subcarrier spacing of the transmission). We include results also for the case where oversampling by $L = 2$ is realized using interpolation of the complex 3MSK sequence instead of phase, in which case $a = 0$ is only included because benefits from using other values of $a$ were not found. The results are shown in Fig. 10 for PAPR at probability levels of 1% and 0.1% and for occupied bandwidth at $-20$ dB and $-30$ dB OOB emission levels. We can see clear benefit of phase interpolation instead of complex signal interpolation especially in the PAPR results. We also see systematic benefit from using $a = 0.05$ instead of $a = 0$ corresponding to linear interpolation with somewhat lower complexity. However, the benefit is rather limited in the interesting cases with low EBW.

It is shown as well that PAPR reduces monotonically with increasing EBW, up to the region where EBW exceeds 90%. This leads to the following interpretation: FFT bins in the excess band help to reduce the PAPR, i.e., each of them reduces the peaks and valleys in the envelope of the generated signal. In cases with $K = N/2$ the PAPR approaches zero dB with increasing EBW. In the theoretical extreme case with $K'' = 2K = N$, the fullband signal has perfectly constant envelope, because DFT-IFFT processing becomes transparent. However, this is not a practical case since the signal at the IFFT output is not spectrally well-contained and channel filtering after analog-to-digital conversion would introduce envelope variations.

With the $-30$ dB OOB emission limit, the occupied bandwidth is close to $K'' \cdot SCS$ with phase interpolation while it saturates to about $1.7 \cdot K \cdot SCS$ with complex signal interpolation. The occupied bandwidths with $-20$ dB OOB emission limit saturate to clearly lower values.

Excess band can be used also in the receiver to improve the link performance. In this case the spectral efficiency reduces further, because the excess bands of adjacent users/allocations cannot be overlapping, if the receivers utilizes the excess band. However, if the excess band does not include all the $L \cdot K$ bins (i.e., if $EBW < 100\%$), both in transmitter and receiver, inter-symbol interference is observed in the receiver.

## IV. RECEIVER PROCESSING

Assuming DFT-s-OFDM transmission as Fig. 1, the receiver processing can be implemented as depicted in Fig. 11, where the blocks highlighted in blue are the additional blocks needed for 3MSK detection.

In the case of a coherent receiver, we use a frequency-domain equalizer (FDE) based on the minimum mean-squared error (MMSE) criterion [21] to compensate the channel effects, while a sequence detector of relatively low complexity is used to detect the 3MSK symbol sequence. It has to be noted that the FDE is not necessary, and this modulation can be decoded with a non-coherent receiver, as will be shown in Section VI.

Different sequence detectors can be used to detect the 3MSK signal. In this work we consider primarily the BCJR algorithm [22]. However it has to be noted, that other types of sequence detectors can be applied as well, e.g.,

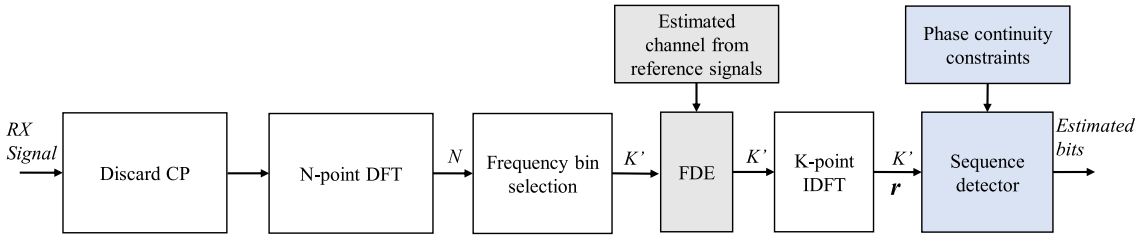


**FIGURE 11.** Block-diagram of the generic 3MSK receiver for DFT-s-OFDM.

the Viterbi algorithm [23] or soft-output Viterbi algorithm (SOVA) [24]. Actually, a modified Viterbi algorithm is used for the uncoded link performance results in Section VI. In the BCJR algorithm used here, states are represented by the 3MSK symbol phases, for instance, 0, $\pm\pi/2$ and $\pi$ rad. One additional functionality that can be added to the detection procedure is a phase error tracking estimate that updates the phase error recursively for each surviving path during the trellis search. This is very useful for mmWave and sub-THz communications, where the PN is very strong and can deteriorate the signal reception quality, especially with low-cost devices [25]. The important characteristic of this receiver processing is that it tracks the phase error by only using data symbols, i.e., no extra reference signals are needed. The addition of the recursive phase error tracking exploits the correlation between consecutive PN samples [26].

For each surviving path, the recursive phase error estimate is updated as

$$\Delta_k^n = (1-\lambda)\cdot\Delta_{k-1}^m + \lambda\cdot\left(\phi_{k,\text{observed}} - \phi_{3\text{MSK}}^n\right), \quad (8)$$

for $m, n \in \{0, 2, \ldots, N_{\text{states}} - 1\}$, where $N_{\text{states}}$ is the number of states in the trellis, $m$ is the previous state (symbol $k-1$) in the surviving path to state $n$ on the $k$th symbol (i.e., the path with the lowest metric of all the paths arriving to the state $n$ at instant $k$), $\phi_{k,\text{observed}}$ is the phase or the $k$th received symbol and $\phi_{3\text{MSK}}^n$ is the phase of the reference 3MSK symbol for state $n$. The constant $\lambda \in [0, 1]$ is the estimation step that controls the recursive update of the phase error, giving more or less weight to the new observation. This phase error estimation can be used to compensate the received samples and improve the detection performance under severe PN degradation.

A simple trellis diagram of the receiver with $N_{\text{states}} = 4$ is shown in Fig. 12. For simplicity, only the forward probabilities ($\alpha$) are shown, but the backward probabilities ($\beta$) can be computed equivalently from the opposite direction. Each state represents a complex-valued 3MSK symbol. Since it is assumed that in the transmitter the bit-to-transition mapping starts in state 0 ($s_0$, which equals symbol value of $1 + 0$j), the only possible states for the first received symbol are $s_0$, $s_1$ and $s_2$. After receiving the first symbol, there are 3 transitions from each state (which are 0 or $\pm\pi/2$). The trellis diagram continues until the end of the 3MSK block. The $\alpha_k(n)$ values represent the probability of being in state $n$ at

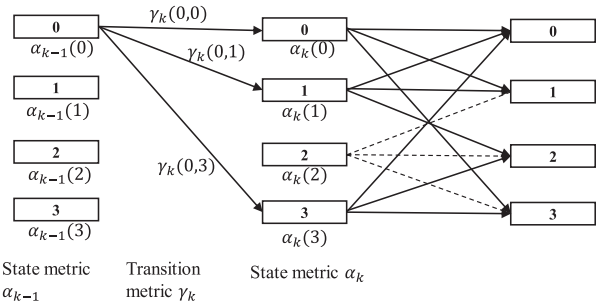


**FIGURE 12.** Example of a simple trellis diagram for the BCJR receiver for 3MSK.

time instant $k$. The updated state value follows the expression

$$\alpha_k(n) = \min\{\alpha_{k-1}(m)\cdot\gamma_k(m,n)\} \quad m, n \in \{0, 1, 2, \ldots, N_{\text{states}} - 1\}, \quad (9)$$

where $\gamma_k(m, n)$ is the transition metric between state $m$ and $n$ at time instant $k$. It can be based for example on Euclidean metric between the received symbol corrected by the conjugate of the phase error estimate, and the 3MSK symbol for state $m$ as

$$\gamma_k(m,n) = \text{dist}\left\{r_k\cdot exp\left(-j\Delta_{k-1}^m\right), exp\left(j\phi_{3\text{MSK}}^n\right)\right\}, \quad (10)$$

where dist$\{\cdot\}$ represents a given distance (it can be for instance Euclidean distance or angular distance). $exp(-j\Delta_{k-1}^m)$ is the phase correction factor from state $m$ in the instant $k-1$, i.e., the last update of phase error estimate, $r_k$ is the received symbol at instant $k$, and $\phi_{3\text{MSK}}^n$ is the phase of the reference 3MSK symbol for state $n$.

Assuming that the 3MSK symbol block is of length $K$ and equal to the DFT length, the phase transition model includes $K + 1$ states, but only $K$ of them are available from the receiver's FFT-IDFT process. Then the idea of equal initial and end states (needed for CP phase continuity) is useful also for the 3MSK signal detection because the selected trellis path would be the one with the lowest metric with the same initial and final state.

For the uncoded BER simulations we use a hard-detection Viterbi decoder while the frequency selective channel is equalized by the FDE. In non-oversampled transmission, a four-state Viterbi detector selects a valid 3MSK symbol sequence with the shortest Euclidean distance, and in case of CP phase continuity, the same initial and end states. In oversampled transmission, additional ISI is introduced as

discussed in Section II-C and we have not found a way to reduce this effect by a linear equalizer. A basic approach is to use non-oversampled receiver processing and the same four-state detector as with the non-oversampled transmitter. Recalling that for each 3MSK symbol, the mean of the ISI-affected symbols has the original phase, just proper scaling of the amplitude of the received signal after the FDE is needed. We have tried to use a 12-state Viterbi detector using the ISI-affected symbol model corresponding to Fig. 7, but the gain in link performance was small compared to the basic non-oversampled receiver. Another approach is to use 2x-oversampled receiver processing with 4-state Viterbi-detector, where the distance metric uses two signal values, at the current symbol time and half-way to the next one. The latter approach turned out to perform better than the 12-state detector, and it is included in the results of Section VI. It should be noted that this scheme can also make use of the excess band in the receiver.

## V. EVALUATION METHODS AND PERFORMANCE METRICS

The performance of this modulation is evaluated from the transmitter and radio link level perspectives. In the transmitter side, the reduced PAPR of the signal with its different variants is evaluated, as well as the spectrum localization, measured in terms of OOB emissions and occupied bandwidth. The maximum transmit power is obtained by taking into account the RF requirements from 5G NR Rel-16 in the frequency range 2 (FR2) defined by 3GPP as the frequency bands between 24250 MHz and 52600 MHz [27]. In addition, radio link level performance evaluations are performed with realistic channel models and with severe phase noise (PN).

### A. PEAK TO AVERAGE POWER RATIO

The PAPR of a signal is a good first metric to measure how efficiently the PA can be used (i.e., how deep into saturation can the PA be driven without causing severe non-linearities that degrade the signal quality). In this work, the instantaneous PAPR of the signal is computed via Monte Carlo simulations as the ratio of the power of each sample to the average power of the signal as

$$PAPR(n) = \frac{|x(n)|^2}{\frac{1}{N_{\text{tot}}} \sum_{l=0}^{N_{\text{tot}}-1} |x(l)|^2}, \tag{11}$$

where $x(n)$ is the value of the $n$th complex sample and $N_{\text{tot}}$ is the signal length in samples. In order to compute the PAPR, a signal with a large number of DFT-s-OFDM blocks is generated. After obtaining the instantaneous PAPR of each signal sample, the statistical distribution is presented with the complementary cumulative distribution function (CCDF) [28].

### B. MAXIMUM ACHIEVABLE TRANSMIT POWER

To evaluate the actual transmitter performance in a more realistic scenario, the maximum output power achievable is obtained after transmitting the signal through a realistic PA model and measuring the different RF emission levels in relation to the limits defined for the 3GPP 5G NR standard with a Rel-16 compliant emission evaluation tool.

More specifically, the RF emission requirements, defined in [27] are: (i) adjacent channel leakage ratio (ACLR) with a limit set to 31 dB, (ii) error vector magnitude (EVM), with a limit of 17.5%, (iii) in-band emission (IBE), following the IBE mask defined in [27], and (iv) occupied bandwidth (OBW), mandating that 99% of the power lies within the allocated bandwidth.

In order to asses the maximum achievable power, the input power of the PA is increased, measuring the PA output power and all the RF emission requirements until some of the requirements is not met.

The results are shown as a function of the output back-off (OBO), which corresponds to the difference in output power with respect to the saturation power of the PA, thus, 0 dB OBO corresponds to a transmission with a fully saturated PA.

### C. LINK LEVEL EVALUATIONS

A final metric to measure the performance of the studied modulation is by means of link level evaluations. For that purpose, the different variations of the 3MSK are transmitted through realistic channel models, and with the presence of PN. Uncoded bit error rate (BER) and coded block error rate (BLER) performance are obtained varying the signal to noise ratio (SNR). The coded performance is obtained by utilizing LDPC codes as defined in [29].

#### 1) CHANNEL MODELS

The channel model used for evaluations is the TDL-E channel model with a delay spread of 50 ns defined in [30].

#### 2) PHASE NOISE MODELS

The PN models used for evaluations are defined in [31], where the UE channel model is used in the transmitter side, and the base station (BS) channel model is used in the receiver side. For the evaluations where PN is included, a carrier frequency of 90 GHz is used, together with a subcarrier spacing (SCS) of 120 kHz.

## VI. NUMERICAL RESULTS

In the results shown in this paper, the size of a 3MSK block is the same as the DFT size. This means that in the non-oversampled (oversampled) case each DFT-s-OFDM block with $K$ ($2K$) in-band frequency bins, carries one 3MSK block of $K$ 3MSK symbols. Table 3 shows the main simulation parameters used.

### A. TRANSMITTER PERFORMANCE

To evaluate the transmitter performance, let us first illustrate the effects of the different parameterization (namely phase continuity, oversampled 3MSK signal generation, EBW utilization, and symmetric/non-symmetric mapping) on the

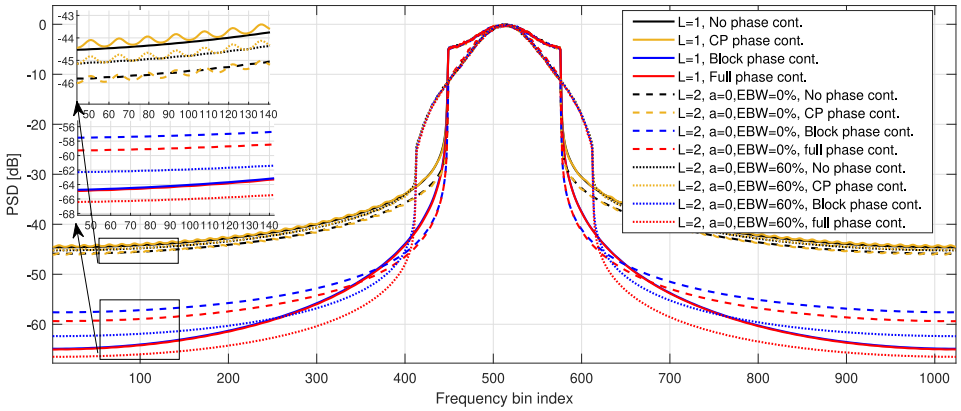


**FIGURE 13.** PSD examples of 3MSK with and without oversampling, for different combinations of phase continuity and excess bandwidth. $K = 128$, IFFT size $N = 1024$. CP length of 128 is used to reach exact block phase continuity.

**TABLE 3.** Main simulation parameters.

| Parameter | Value |
|---|---|
| Phase continuity | No phase continuity, CP-main block, between DFT-s-OFDM blocks, and full phase continuity |
| Subcarrier spacing | 120 kHz |
| Channel model | TDL-E [30] |
| Phase noise model | PN models from [31] |

power spectral density (PSD) of the signal. Fig. 13 shows the PSD of the signal with different types of phase continuity (phase continuity between CP and main block, phase continuity between consecutive DFT-s-OFDM blocks, and full phase continuity), as well as oversampling factors of 1 and 2, with different usage of the excess band. It is important to note that Fig. 13 illustrates the effects when exact phase continuity is used between DFT-s-OFDM blocks (i.e., $\phi_t^{\text{diff}}$ is a multiple of $\pi/2$ in (2)). It is observed that two groups can be differentiated, based on the types of phase continuity.

### 1) NO PHASE CONTINUITY AND CP PHASE CONTINUITY

On one side, the group with higher OOB emissions is formed with the cases when no phase continuity is used, or when only CP phase continuity is used, irrespective of what is the oversampling factor or the usage of EBW. It can be seen that in this group, the combination providing the lowest OOB emissions corresponds to the case when oversampling is used without EBW utilization. An important observation is that CP to main block phase continuity alone provides very minor benefit in OOB emission and may even increase it. So the main benefit in terms of OOB emissions is that it enhances to effect of block phase continuity, as discussed in Section II-B.

### 2) BLOCK PHASE CONTINUITY AND FULL PHASE CONTINUITY

The group with the lowest OOB emissions is formed with the cases when the phase continuity between DFT-s-OFDM blocks is used, and the cases when full phase continuity is used. As expected, with full phase continuity, the OOB emissions for both oversampling factors are the lowest of all the tested cases. However, in the 2-times oversampled case, we have more control over the phase behavior and visible effects can be seen when full phase continuity is utilized, compared to the case of just block phase continuity. An important observation is that with $L = 2$, the PSD decays faster when going away from the in-band frequency bins, but further from the in-band $L = 1$ presents lower OOB emissions.

Additionally, we study the effects of exact vs. approximate phase continuity between DFT-s-OFDM blocks. Recall that the condition for exact block phase continuity is that, $\phi_t^{\text{diff}}$ is a multiple of $\pi/2$, which is achieved when the CP-length is formed by an integer number of 3MSK symbols.

The comparison of exact and non-exact phase continuity between DFT-s-OFDM blocks is illustrated in Fig. 14. It can be seen that when the phase continuity is exact, the OOB emissions can be reduced between 5 and 10 dB, compared to the case of approximate block phase continuity. It has to be noted that although approximated phase continuity between DFT-s-OFDM blocks is not as effective as exact phase continuity, it still reduces the OOB emissions by up to 10 dB with respect to the case where no phase continuity is enforced (see Fig. 13).

The two different parameterizations for exact block phase continuity in Fig. 13 and Fig.14 reach similar benefits in terms of OOB emissions. In Fig. 13 the 3MSK symbol duration is integer $N/K = 1024/128 = 8$ and any multiple of 8 as CP length satisfies the condition for exact block phase continuity. In Fig. 14 the 3MSK symbol duration is $N/K = 1024/120 = 128/15$ and the smallest feasible CP length is 128.

Finally, Fig. 15 compares the non-symmetric bit-to-transition mapping with symmetric mapping (SM). It can be seen that the NSM presents lower OOB emissions that the SM due to the smoother phase variations.

To better characterize the effects of the different options, Fig. 16 illustrates the comparisons of the PAPR distributions of the 3MSK signal applied on DFT-s-OFDM, compared to

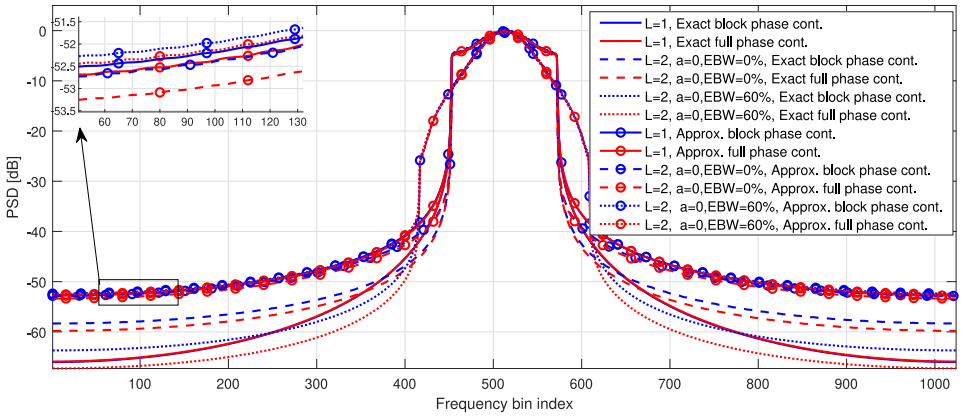


**FIGURE 14.** PSD examples of 3MSK for exact phase continuity between DFT-s-OFDM blocks and non-exact phase continuity between DFT-s-OFDM blocks. $K = 120$, IFFT size $N = 1024$. For exact phase continuity between CP-OFDM blocks, the CP length is 128 samples, and for approximated phase continuity between CP-OFDM blocks, the CP length is 72 samples.

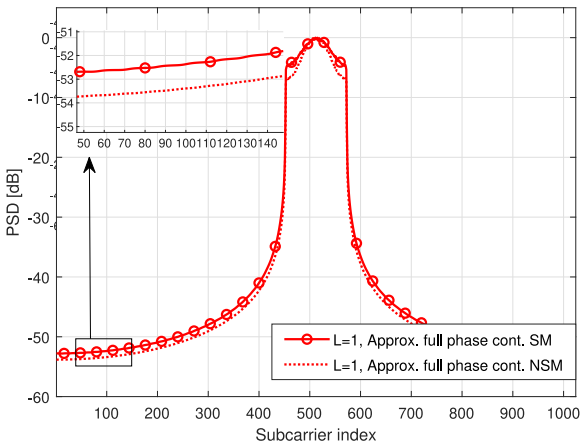


**FIGURE 15.** PSD examples of 3MSK for $L = 1$ comparing non-symmetric mapping with symmetric mapping with approximate full phase continuity.

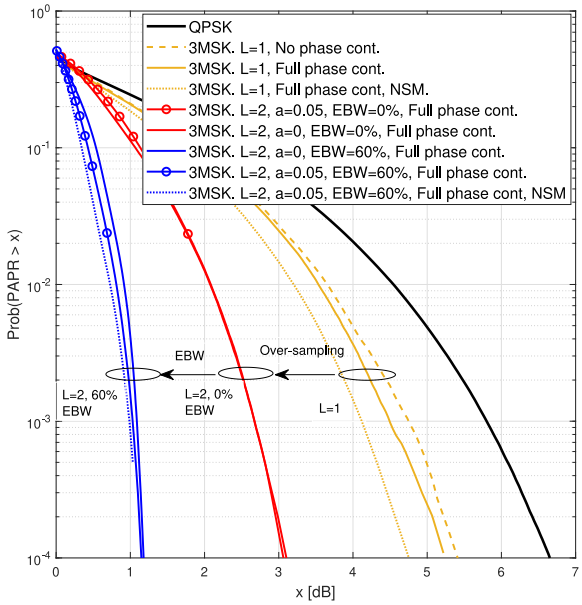


**FIGURE 16.** Example of PAPR CCDF distributions with and without oversampling, with different excess bandwidths (EBWs).

QPSK. It can be seen that the basic 3MSK transmission without oversampling or EBW already presents lower PAPR than QPSK (1 dB lower at $10^{-2}$ CCDF probability point). It has to be noted that if NSM is used, the PAPR can be reduced further by 0.3 dB with respect to the symmetric mapping with full phase continuity. This is because NSM favors smoother phase variations when transition pair $+\pi/2, -\pi/2$ (or $-\pi/2, +\pi/2$) is discarded, instead of the transition pair $0, 0$ in the symmetric mapping.

The PAPR can be further reduced with the aid of oversampling, where up to 1.5 dB lower PAPR at $10^{-2}$ CCDF probability point can be achieved if $L = 2$ and no EBW is used. Furthermore, increasing the EBW from 0% to 60% further reduces the PAPR down to 0.7 dB, at the expense of spectrum efficiency loss.

Next we compare the PAPR and OOB emission performance of 3MSK against the $\pi/2$ BPSK based schemes included in the comparison of [18]. Here the PAPR comparison is based on OFDM block based PAPR metric, instead of the sample based one used elsewhere in this paper.

**TABLE 4.** PAPR comparison of the proposed 3MSK modulation and the schemes of [16], [18], [32], [33].

| Scheme | PAPR @1% Probability | | |
|---|---|---|---|
| | **Basic scheme** | **0 EBW** | **50% EBW** |
| **3MSK** $L = 1$ | **5.2 dB** | N/A | N/A |
| $\pi/2$ BPSK | 5.1 dB | N/A | N/A |
| **3MSK** $L = 2$ | N/A | **3.1 dB** | **1.3 dB** |
| Schemes of [32] and [33] | N/A | 1.5 - 2.1 dB | N/A |
| FDSS with RRC weights | N/A | N/A | 2.3 dB |
| Schemes of [16] and [18] | N/A | N/A | 0.6-0.9 dB |

The PAPR values are shown in Table 4 at 1% probability level.

The main parameters are $N = 1024$, $K = 24$ (2 physical resource blocks (PRBs)), and the excess bandwidth is 50% when applied. In the non-oversampled case, 3MSK achieves

**TABLE 5.** OOB bandwidth comparison of the proposed 3MSK modulation and the schemes of [16], [18], [32], [33] with linear PA.

| Scheme | Normalized bandwidth | |
|---|---|---|
| | -20 dB OOB | -30 dB OOB |
| **3MSK $L = 1$** | **1** | **1.33** |
| $\pi/2$BPSK | 1.18 | >>2.5 |
| **3MSK $L = 2$, 0% EBW** | **1** | **1.25** |
| Schemes of [32] and [33] | 0.95-1 | >>2.5 |
| **3MSK $L = 2$, 50% EBW** | **1.25** | **1.5** |
| FDSS with RRC | 1.38 | >>2.5 |
| Schemes of [18] and [16] | 1.20-1.26 | >>2.5 |

similar PAPR performance as basic $\pi/2$ BPSK, and in oversampled cases without excess band, up to 1.6 dB higher PAPR than enhanced $\pi/2$ BPSK based schemes without excess band. With 50% excess, 3MSK has about 0.5 dB higher PAPR than the best binary schemes presented in [18] having the same excess band.

Regarding OOB emissions, Table 5 shows the occupied bandwidths for $-20$ dB and $-30$ OOB power ratios for the same modulation schemes while assuming ideal (linear) power amplifier. We can observe that the occupied bandwidth of 3MSK is rather similar to the best $\pi/2$ BPSK based schemes at 1% OOB emission level, but much better at lower OOB emission levels. The $-20$ dB OOB power ratio is reached outside the band of $K = 24$ frequency bins (normalized bandwidth of 1) both in non-oversampled and oversampled cases of 3MSK without excess band, and outside $K + 6 = 30$ frequency bins (i.e., normalized bandwidth of 1.25) when 50% excess band is applied. These values are similar to best schemes included in the comparisons of [18] in terms of OOB emissions. Furthermore, $-30$ dB OOB power ratio is reached with normalized bandwidth of 1.33 in non-oversampled case, 1.25 in oversampled case without excess band, 1.5 with 50% excess band, while the corresponding normalized bandwidth is beyond 2.5 in all cases included in [18].

Table 6 shows the occupied bandwidth in terms of normalized bandwidth for the different phase continuity and EBW configurations of 3MSK, with different values of the parameter $a$. A linear (ideal) PA is used to obtain the reference values, and a modified Rapp model from [34] with an input backoff (IBO) of 0.5 dB is used to evaluate the signal with non-linear PA. It can be seen that modifying the parameter $a$ of the interpolation filter has a very minor effect on spectrum localization. An important result, showed in Fig. 13 as well, is that full phase continuity has a significant effect in terms of occupied bandwidth.

Finally, a way to evaluate the effects of the PAPR reduction on the signal is to use a realistic PA model and consider the different RF requirements that the signal needs to comply with (namely ACLR, EVM, IBE, OBE, and OBW) in order to obtain what is the maximum output power after the amplification stage. Fig. 17 shows the simulated OBO with respect to the PA saturation point, for an FR2 PA [34] for 3MSK with and without oversampling and QPSK, with respect to the number of allocated PRBs. One PRB corresponds to

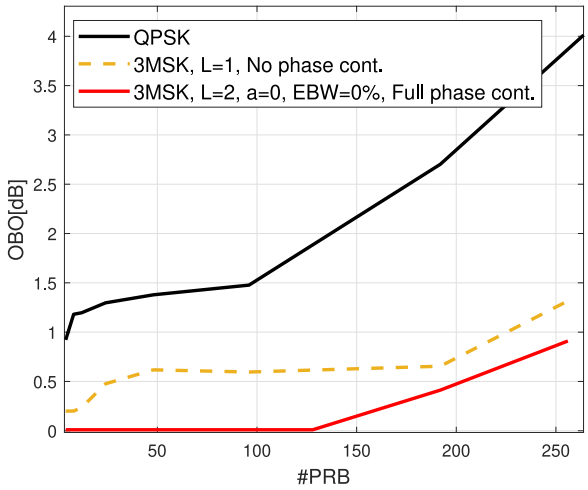


**FIGURE 17.** Simulated achievable OBO comparison between QPSK and 3MSK.

12 frequency bins, or resource elements (RE), in 3GPP nomenclature. It is shown that the basic 3MSK without oversampling can already output up to 3 dB higher power than QPSK when the channel is fully allocated, and 1 dB more for small allocations. Furthermore, with $L = 2$ and full phase continuity the PA can be driven to full saturation for small and medium size allocations, and with full allocation, extra 0.4 dB output power compared to non-oversampled case can be obtained, while fulfilling all the RF emission requirements.

### *B. RADIO LINK LEVEL EVALUATIONS*

In order to asses the performance of the 3MSK, several radio link level simulations have been evaluated under different conditions to compare the performance of the different variants of 3MSK in terms of uncoded BER with a coherent receiver. These conditions include additive white Gaussian noise (AWGN) channel and TDL-E channel model defined in [30] with delay spread of 50 ns. Additionally, PN degradation is included in the simulations to show the robustness of the receiver processing against the effect of PN by using the models defined in [31], where the phase tracking step of the 3MSK receiver is set to $\lambda = 0.05$. Finally, a comparison of BLER is presented for 3MSK using non-coherent receiver in the presence of PN. Here the information is encoded with LDPC codes as defined in [29] for the physical uplink shared channel (PUSCH) of 5G NR.

First we evaluate in Figs. 18, 19, and 20 the uncoded BER performance of 3MSK with different transmitter and receiver oversampling factors, excess bandwidths (EBW $= 0$ or EBW $= 50\%$), and interpolation coefficients ($a = 0$ or $a = 0.05$) considering both AWGN and TDL-E channels. With oversampled transmission ($L_{TX} = 2$), $L_{RX} = 1$ indicates the use of basic 4-state Viterbi detection, in which case the possible excess band is discarded in the receiver, and adjacent users' excess bands may be overlapping. $L_{TX} = L_{RX} = 2$ denotes using oversampled Viterbi detector, as explained in

**TABLE 6.** Occupied bandwidth in terms of normalized bandwidth for different phase continuity (PC) and EBW configurations.

| | @-20 dB | | @-30 dB | |
|---|---|---|---|---|
| | **Linear PA** | **IBO=0.5 dB** | **Linear PA** | **IBO=0.5 dB** |
| $L = 1$, no PC | 1.17 | 1.92 | $> 4$ | $> 4$ |
| $L = 1$, full PC | 1 | 1.42 | 1.33 | 2.67 |
| $L = 2$, EBW=0%, no PC, a = 0 | 1.08 | 1.42 | $> 4$ | $> 4$ |
| $L = 2$, EBW=0%, full PC, a = 0 | 1 | 1 | 1.25 | 2 |
| $L = 2$, EBW=0%, no PC, a = 0.05 | 1.08 | 1.42 | $> 4$ | $> 4$ |
| $L = 2$, EBW=0%, full PC, a = 0.05 | 1 | 1.08 | 1.25 | 2.08 |
| $L = 2$, EBW=50%, no PC, a = 0 | 1.42 | 1.5 | $> 4$ | $> 4$ |
| $L = 2$, EBW=50%, full PC, a = 0 | 1.25 | 1.25 | 1.5 | 2.17 |
| $L = 2$, EBW=50%, no PC, a = 0.05 | 1.42 | 1.5 | $> 4$ | $> 4$ |
| $L = 2$, EBW=50%, full PC, a = 0.05 | 1.25 | 1.25 | 1.5 | 2.08 |

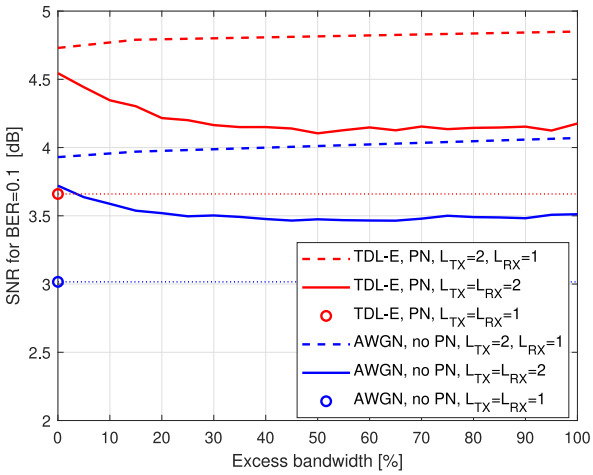


**FIGURE 18.** Required SNR for 10% uncoded BER as a function of excess bandwidth for oversampled and non-oversampled receivers with $N = 1024$, $K = 120$, full phase continuity, and $a = 0.05$.

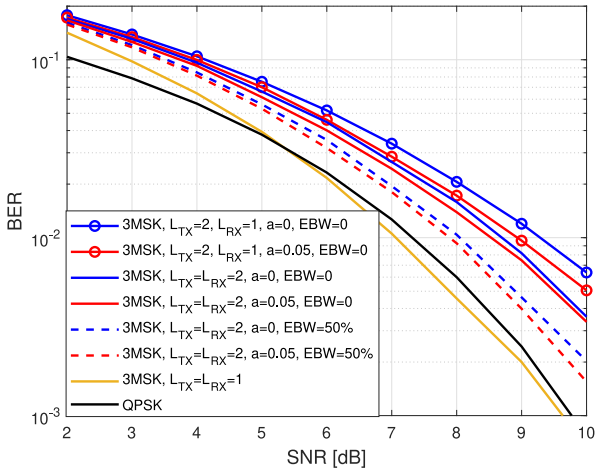


**FIGURE 19.** Uncoded link level results for AWGN channel with $K = 12$, full phase continuity, different *a*-coefficients, different transmitter and receiver oversampling factors, and excess bandwidths.

Section IV, and overlapping excess bands are not feasible. Generally, it was observed that phase continuity has minor effect on the link performance and all BER results here are with full phase continuity.

Fig. 18 shows the effect of excess bandwidth in oversampled transmission at 10% BER level for the two alternative receivers and both channel models, with the non-oversampled case as reference. We can see that the oversampled receiver provides clear benefit with modest and wide excess bands. The SNR gain is 0.5 dB or more when EBW = 20% or higher. It is interesting to note that there is some benefit (about 0.2 dB) even with zero excess band. When using the oversampled receiver, the link performance loss with respect to non-oversampled transmission is 0.4-0.8 dB, depending on the excess bandwidth, for both channel models.

Fig. 19 shows the uncoded BER with AWGN channel for the 3MSK variants, with QPSK as reference. It is worth to note that with $a = 0.05$, the BER is somewhat lower than with $a = 0$ and the SNR gain due to 50% excess band increases with increasing SNR. It can be observed that the uncoded BER of 3MSK with $L = 1$ is rather similar to that of QPSK. The BER is plotted here in terms of SNR, which could potentially be higher for 3MSK than for QPSK with the same PA. This is due to the fact that considerably lower backoff can be used compared to QPSK, resulting in higher transmission power while remaining within the OOB emission requirements. This gain is due to the reduced PAPR, but this extra power gain is not included in the SNR based comparisons.

Fig. 20 shows the uncoded BER with TDL-E channel for the 3MSK variants with EBW=0 and $a = 0.05$, with QPSK as reference. For the 3MSK, the degradation when PN is included with $L = 1$ is about 0.6 dB at the 1% BER point, while the corresponding degradation for QPSK is about 1.3 dB, and 3MSK with $L = 1$ performs 1 dB better than QPSK at 1% BER level when PN is present. At 10% BER level, QPSK is about 0.6 dB better than 3MSK with $L = 1$. We can also see that, with oversampled transmission, an oversampled receiver has minor benefit with severe PN but in case of TDL-E channel without PN, the benefit is more significant. In this case, 3MSK with oversampled transmitter and receiver needs 1.4 dB higher SNR than QPSK at 10% BER level and 0.8 dB higher at 1% BER level, which are lower than the extra output power gain that could be obtained from the oversampled transmitter.

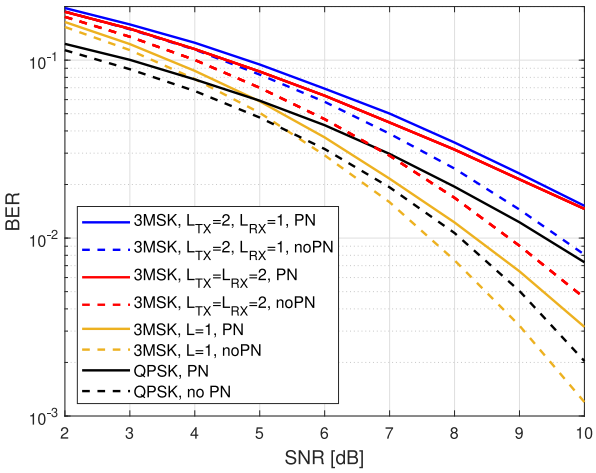


**FIGURE 20.** Uncoded link level results for TDL-E channel with and without PN, with $K = 120$, full phase continuity, $a = 0.05$, EBW=0, and different transmitter and receiver oversampling factors.

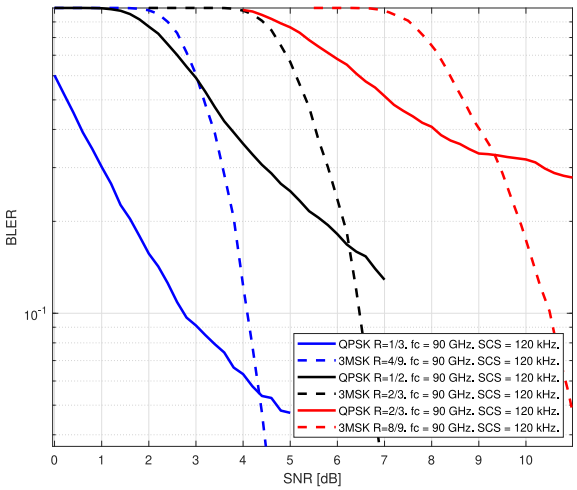


**FIGURE 21.** Coded Link level results for TDL-E channel with non-coherent receiver.

Finally, Fig. 21 shows the coded link level results for 3MSK with oversampling factor $L = 1$ and QPSK when non-coherent reception is assumed and PN is included. The coding rates of 3MSK and QPSK are paired in such a way that both transmissions have the same spectral efficiency. This means that the equivalent coding rate of 3MSK is increased by the factor of $2/1.5 = 1.33$ to ensure same spectral efficiency. For 3MSK, the phase error tracking step in the receiver, $\lambda$, is set to 0.05. It can be seen how the 3MSK transmissions is able to reach the $10^{-1}$ BLER point even with non-coherent receiver and severe PN degradation, while QPSK presents an error floor at higher coding rates, proving the resilience of 3MSK to PN impairments.

## VII. CONCLUSION

In this article, a novel DFT-s-OFDM based waveform with 3-level CPM based modulation scheme, referred to as 3MSK, was proposed and shown to provide well-localized spectrum, low PAPR, and robustness against phase noise, while also facilitating non-coherent receiver processing and low processing complexity. It was observed that phase continuity between underlying CP-OFDM blocks helps to reduce the out-of-band emissions greatly. In terms of occupied bandwidth metric, 3MSK was found to exceed the performance of best $\pi/2$ BPSK based DFT-s-OFDM reference schemes, also when a practical nonlinear power amplifier model is included. On the other hand, phase continuity between CP and main block, having clear effect on OOB emissions only in oversampled cases, has minor importance from the spectrum localization point of view. However, it helps to reduce PAPR in some scenarios, and most importantly, it helps to deal with phase uncertainty in the phase rotation based block phase continuity scheme, leading to improved link performance. Therefore, schemes with full phase continuity appear as the most interesting choice.

Oversampled signal generation and utilization of excess band was found to greatly improve the PAPR characteristics, reaching the PAPR of common $\pi/2$ BPSK schemes. One important advantage of the PAPR reduction can be seen in the results of maximum output power achievable from a realistic PA, where non-oversampled 3MSK can outperform QPSK by 3 dB, and with $L = 2$, fully saturated PA can be used. The use of smoother 7-tap phase interpolation filter instead of linear interpolation provides worthwhile improvement both in PAPR and link performance. Finally, coded link level performance results were presented, showing that 3MSK without oversampling has similar performance to that of QPSK, and that in strong PN scenarios, 3MSK can be detected without the need of extra reference signals.

In the non-oversampled case, significant reduction in the occupied bandwidth is obtained with low additional computational complexity through enhanced phase continuity. The most significant limitation/tradedoff of the proposed oversampled scheme is that the improvements of PAPR and achievable transmission power are obtained at the cost of loss in the link performance (e.g., 0.4 – 0.8 dB loss with the oversampled receiver at the uncoded BER level of 10%) compared to the non-oversampled case. Another obvious tradeoff is that the use of excess band reduces spectrum localization. Oversampling leads to doubling of the DFT length, which is significant in wideband allocations (say when $K > N/4$), but minor additional complexity in narrowband cases. Otherwise, while certain additional signal processing functions are needed both in the transmitter and the receiver, their computational complexity is low compared to the DFT-s-OFDM processing.

Overall, 3MSK was found to provide new and interesting tradeoffs between data rate and achievable transmission power with effective and low-cost power amplifiers, as an alternative to binary and 4-level transmission schemes. The views of future research include possibilities to reduce the gap in the link performance between basic and oversampled models through improved detection methods, considering both cases with and without excess band in the transmitter, as well as more effective utilization of the excess band

in the receiver. The oversampled transmitter and receiver approaches were mainly evaluated experimentally, so developing analytical models for these schemes remains as an important topic for future studies.

## REFERENCES


[1] L. Chettri and R. Bera, "A comprehensive survey on Internet of Things (IoT) toward 5G wireless systems," *IEEE Internet Things J.*, vol. 7, no. 1, pp. 16–32, 2020.

[2] R. Mozny, M. Stusek, P. Masek, K. Mikhaylov, and J. Hosek, "Unifying multi-radio communication technologies to enable mMTC applications in B5G networks," in *Proc. 2nd 6G Wireless Summit (6G SUMMIT)*, 2020, pp. 1–5.

[3] A. Hoeller, J. Sant'Ana, J. Markkula, K. Mikhaylov, R. Souza, and H. Alves, "Beyond 5G low-power wide-area networks: A LoRaWAN suitability study," in *Proc. 2nd 6G Wireless Summit (6G SUMMIT)*, 2020, pp. 1–5.

[4] U. Raza, P. Kulkarni, and M. Sooriyabandara, "Low power wide area networks: An overview," *IEEE Commun. Surveys Tuts.*, vol. 19, no. 2, pp. 855–873, 2nd Quart., 2017.

[5] P. Annamalai, J. Bapat, and D. Das, "Emerging access technologies and open challenges in 5G IoT: From physical layer perspective," in *Proc. IEEE Int. Conf. Adv. Netw. Telecommun. Syst. (ANTS)*, 2018, pp. 1–6.

[6] I. P. Nasarre, T. Levanen, K. Pajukoski, A. Lehti, E. Tiirola, and M. Valkama, "Enhanced uplink coverage for 5G NR: Frequency-domain spectral shaping with spectral extension," *IEEE Open J. Commun. Soc.*, vol. 2, pp. 1188–1204, 2021.

[7] M. Kanj, V. Savaux, and M. Le Guen, "A tutorial on NB-IoT physical layer design," *IEEE Commun. Surveys Tuts.*, vol. 22, no. 4, pp. 2408–2446, 4th Quart., 2020.

[8] (LoRa Alliance, Beaverton, OR, USA). *LoRaWAN Specification*, (2016). [Online]. Available: https://lora-alliance.org/lorawan-for-developers/ (accessed Sep. 10, 2021).

[9] I. Demirkol, C. Ersoy, and F. Alagoz, "MAC protocols for wireless sensor networks: A survey," *IEEE Commun. Mag.*, vol. 44, no. 4, pp. 115–121, Apr. 2006.

[10] M. L. Doelz and E. H. Head, "Minimum-shift data communication system," U.S. Patent 2 977 417, 1961.

[11] J. G. Proakis and M. Salehi, *Digital Communications*, 5th ed. New York, NY, USA: McGraw-Hill.

[12] S. Pasupathy, "Minimum shift keying: A spectrally efficient modulation," *IEEE Commun. Mag.*, vol. 17, no. 4, pp. 14–22, Jul. 1979.

[13] K. Murota and K. Hirade, "GMSK modulation for digital mobile radio telephony," *IEEE Trans. Commun.*, vol. 29, no. 7, pp. 1044–1050, Jul. 1981.

[14] A. Z. Mohammed, A. K. Nain, J. Bandaru, A. Kumar, D. S. Reddy, and R. Pachamuthu, "A residual phase noise compensation method for IEEE 802.15.4 compliant dual-mode receiver for diverse low power IoT applications," *IEEE Internet Things J.*, vol. 6, no. 2, pp. 3437–3447, Apr. 2019.

[15] *IEEE Standard for Low-Rate Wireless Networks*, IEEE Standard 802.15.4-2020 (Revision of IEEE Std 802.15.4-2015), 2020.

[16] J. Kim, Y. H. Yun, C. Kim, and J. H. Cho, "Minimization of PAPR for DFT-spread OFDM With BPSK symbols," *IEEE Trans. Veh. Technol.*, vol. 67, no. 12, pp. 11746–11758, Dec. 2018.

[17] H. G. Myung, J. Lim, and D. J. Goodman, "Single carrier FDMA for uplink wireless transmission," *IEEE Veh. Technol. Mag.*, vol. 1, no. 3, pp. 30–38, Sep. 2006.

[18] J. Choi, J. H. Cho, and J. S. Lehnert, "Continuous-phase modulation for DFT-spread localized OFDM," *IEEE Open J. Commun. Soc.*, vol. 2, pp. 1405–1418, 2021.

[19] I. Peruga Nasarre, T. Levanen, and M. Valkama, "Constrained PSK: Energy-efficient modulation for sub-THz systems," in *Proc. IEEE Int. Conf. Commun. Workshops (ICC Workshops)*, 2020, pp. 1–7.

[20] M. P. Wylie-Green, E. Perrins, and T. Svensson, "Introduction to CPM-SC-FDMA: A novel multiple-access power-efficient transmission scheme," *IEEE Trans. Commun.*, vol. 59, no. 7, pp. 1904–1915, Jul. 2011.

[21] B. E. Priyanto, H. Codina, S. Rene, T. B. Sorensen, and P. Mogensen, "Initial performance evaluation of DFT-spread OFDM based SC-FDMA for UTRA LTE uplink," in *Proc. IEEE 65th Veh. Technol. Conf.*, 2007, pp. 3175–3179.

[22] L. Bahl, J. Cocke, F. Jelinek, and J. Raviv, "Optimal decoding of linear codes for minimizing symbol error rate (corresp.)," *IEEE Trans. Inf. Theory*, vol. 20, no. 2, pp. 284–287, Mar. 1974.

[23] A. Viterbi, "Error bounds for convolutional codes and an asymptotically optimum decoding algorithm," *IEEE Trans. Inf. Theory*, vol. 13, no. 2, pp. 260–269, Apr. 1967.

[24] J. Hagenauer and P. Hoeher, "A Viterbi algorithm with soft-decision outputs and its applications," in *Proc. IEEE Global Telecommun. Conf. Exhibition Commun. Technol. Beyond*, vol. 3, 1989, pp. 1680–1686.

[25] M. Rezaei and K. M.-P. Aghdam, "Phase noise reduction in low cost 24/77 GHz FMCW sensors," in *Proc. 18th Mediterr. Microw. Symp. (MMS)*, 2018, pp. 229–232.

[26] P. Maffezzoni, F. Pepe, and A. Bonfanti, "A unified method for the analysis of phase and amplitude noise in electrical oscillators," *IEEE Trans. Microw. Theory Techn.*, vol. 61, no. 9, pp. 3277–3284, Sep. 2013.

[27] *User Equipment (UE) Radio Transmission and Reception; Part 2: Range 2 Standalone, Technical Specification Group Radio Access Network, Release-16, V16.2.0*, 3GPP Standard TS 38.101-2, Dec. 2019.

[28] Y. Wang and Z. Luo, "Optimized iterative clipping and filtering for PAPR reduction of OFDM signals," *IEEE Trans. Commun.*, vol. 59, no. 1, pp. 33–37, Jan. 2011.

[29] *5G; NR; Multiplexing and Channel Coding, V16.6.0 Release 16*, 3GPP Standard TS 38.212, Aug. 2021.

[30] "Study on channel model for frequencies from 0.5 to 100 GHz; technical specification group radio access network, V15.1.0," 3GPP, Sophia Antipolis, France, Rep. TR 38.901, Sep. 2019.

[31] "Study on new radio access technology; RF and co-existence aspects (release 14), v2.0.0," 3GPP, Sophia Antipolis, France, Rep. TR 38.803, Mar. 2017.

[32] K. Kuchi, "Partial response DFT-precoded-OFDM modulation," *Eur. Trans. Telecommun.*, vol. 23, no. 7, pp. 632–645, 2012.

[33] *Additional Simulation Results on Low PAPR RS*, document R1-1901117, 3GPP TSG RAN WG1 Ad-Hoc Meeting, 3GPP, Sophia Antipolis, France, Jan. 2019.

[34] *IEEE P802.11 Wireless LANs, TGad Evaluation Methodology*, document IEEE 802.11-09/0296r16, IEEE, Piscataway, NJ, USA, Jan. 2009.


**MARKKU RENFORS** (Life Fellow, IEEE) received the D.Sc. (Tech.) degree from the Tampere University of Technology (TUT), Finland, in 1982. Since 1992, he has been a Professor with TUT (currently Tampere University), since 2020 as a Professor Emeritus. He was the Head of the Department of Electronics and Communications Engineering from 1992 to 2010. His research interests include communication waveforms, multicarrier systems, and signal processing algorithms for communications receivers and transmitters. He was a co-recipient of the Guillemin-Cauer Award (together with T. Saramäki) from the IEEE Circuits and Systems Society in 1987.

**ISMAEL PERUGA NASARRE** received the B.Sc. and M.Sc. degrees from the University of Zaragoza, Spain, in 2017 and 2019, respectively. He was with the Department of Electrical Engineering, Tampere University, Finland, from 2019 to 2021. He is currently with Nokia, Finland. His current research interests include physical-layer design for mobile communications, 5G advanced for coverage enhancements, and mmWave and sub-THz communications.

**TONI LEVANEN** received the M.Sc. and D.Sc. degrees from the Tampere University of Technology, Finland, in 2007 and 2014, respectively. He is currently with Nokia Mobile Networks, Finland. In addition to his contributions in academic research, he has worked in industry on wide variety of development and research projects. His current research interests include physical-layer design for 5G NR, interference modeling in 5G cells, and high-mobility support in millimeter-wave communications.

**KARI PAJUKOSKI** received the B.S.E.E. degree from the Oulu University of Applied Sciences in 1992. He is a Fellow of Nokia Bell Labs. He has a broad experience from cellular standardization, link and system simulation, and algorithm development for products. He has more than 100 issued U.S. patents, from which more than 50 have been declared "standards essential patents." He is the author or coauthor of more than 300 standards contributions and 30 publications, including conference proceedings, journal contributions, and book chapters.

**MIKKO VALKAMA** (Fellow, IEEE) received the M.Sc. (Tech.) and D.Sc. (Tech.) degrees (both with Hons.) from the Tampere University of Technology (TUT), Finland, in 2000 and 2001, respectively. In 2003, he was with the Communications Systems and Signal Processing Institute, SDSU, San Diego, CA, USA, as a Visiting Research Fellow. He is currently a Full Professor and the Head of the Unit of Electrical Engineering at Tampere University, Finland. His general research interests include radio communications, radio localization, and radio-based sensing, with particular emphasis on 5G and 6G mobile radio networks.